electronics

Article

Quantitative Evaluation of Neurite Morphology Using Graph Structure

Fumiya Chikudo [1], Stefan Baar [1], Ayaka Ota [2], Masahiro Kuragano [2,3], Kiyotaka Tokuraku [2] and Shinya Watanabe [1,*]

[1] Division of Information and Electronic Engineering, Muroran Institute of Technology, Mizumoto-cho 27-1, Muroran 050-8585, Japan; 22043040@muroran-it.ac.jp (F.C.); sbaar@muroran-it.ac.jp (S.B.)
[2] Division of Sustainable and Environmental Engineering, Muroran Institute of Technology, Mizumoto-cho 27-1, Muroran 050-8585, Japan; 22041016@muroran-it.ac.jp (A.O.); gano@muroran-it.ac.jp (M.K.); tokuraku@muroran-it.ac.jp (K.T.)
[3] Graduate School of Engineering, Muroran Institute of Technology, Mizumoto-cho 27-1, Muroran 050-8585, Japan
* Correspondence: sin@muroran-it.ac.jp; Tel.: +81-143-46-5432

Abstract: Recently, the analysis of cellular images, particularly the assessment of neurite activity, has gained increasing significance in the study of neurodegenerative diseases, including Alzheimer's disease. This study introduces an automated analysis approach that focuses on neurite activity through the application of cellular segmentation techniques to bright-field images of neurons. This study proposes a method for treating individual cell instances as graphs consisting of nodes and edges. Furthermore, this study suggests a quantitative assessment for precisely identified neurites through the definition of several evaluation metrics. This approach enables the fast and objective automated analysis of bright-field images focused on neurons. In a variety of experiments, the precision of our proposed method was verified through a comparative analysis by comparing the results to manual analysis data using ImageJ for measuring the neurite length of rat adrenal pheochromocytoma PC12 cells. The findings revealed that the average discrepancy in the length of neurites is only 4.387 µm, highlighting the high level of accuracy in our method's ability to detect neurites, which is almost on par with manual analysis. This observation holds significance in analytical applications pertinent to Alzheimer's disease.

Keywords: Alzheimer's disease; image processing; graph structure; quantitative evaluation; high-throughput screening; neurite degeneration; neurite outgrowth

check for updates

Citation: Chikudo, F.; Baar, S.; Ota, A.; Kuragano, M.; Tokuraku, K.; Watanabe, S. Quantitative Evaluation of Neurite Morphology Using Graph Structure. *Electronics* **2023**, *12*, 4750. https://doi.org/10.3390/electronics12234750

Academic Editors: Xin Ning and Ruifan Li

Received: 14 October 2023
Revised: 16 November 2023
Accepted: 21 November 2023
Published: 23 November 2023

Copyright: © 2023 by the authors. Licensee MDPI, Basel, Switzerland. This article is an open access article distributed under the terms and conditions of the Creative Commons Attribution (CC BY) license (https://creativecommons.org/licenses/by/4.0/).

1. Introduction

Alzheimer's disease (AD) is a progressive neurodegenerative disease that was first documented by Alzheimer in 1906 [1]. It is characterized by a gradual decline in cognitive functions, including thinking, memory, and language abilities [2]. Because AD progresses with age, the global prevalence of AD has significantly increased in recent years [3,4]. The etiology of AD is associated with the aggregation of a peptide known as amyloid-β (Aβ) within the brain. This is known as the amyloid cascade hypothesis, and the pathogenesis of AD revolves around the accumulation and aggregation of Aβ in the brain, leading to the aggregation and accumulation of tau proteins, ultimately resulting in neurodegeneration and cell death [5,6].

Therefore, it is essential to evaluate the complex relationship between AD and Aβ to elucidate the underlying mechanisms of AD and advance the development of therapeutic and preventive interventions. To assess this relationship, it is important to investigate the effects of Aβ on brain neurons. Specifically, Aβ, which is considered a causative factor in AD, influences the state and mobility of neurites. For example, Aβ can alter the neurite length, the number of neurite branches, as well as the number of neurite tips and roots.

Among these metrics, the neurite length is the most widely used metric in this field to evaluate neuronal health [7,8]. In recent studies on neurites, basic metrics, such as neurite length, neurite area, and the number of branches, have been employed [9,10]. These traditional metrics, though they are straightforward, yield highly valuable information.

In the process of evaluating neurons with respect to these metrics during long-term microscopic time-lapse observations, it is important to assess the cell status, with a specific focus on neurite activity. Given that neurite activity serves as the most informative aspect for estimating neuronal dynamics, it can be employed to scrutinize any symptoms of the effects on cellular activity. Therefore, in the assessment of cell states and neuronal dynamics, the development of effective tools and methodologies for quantitatively evaluating neurite activity is very important.

Currently, the software tools widely used for cell analysis include support tools like ImageJ (ver.1.53) [11] and CellProfiler (ver.4.2.1) [12]. However, these analysis support tools require a lot of human work, and even when examining the same image, the results may differ greatly depending on the analyst. Additionally, when dealing with videos, manual work is often required for each frame, demanding a substantial effort, and introducing subjectivity. Tools such as NeuriteTracer [13] have been developed for semi-automatic cell analysis, with a particular focus on neurons. Moreover, fully automated analysis tools, such as NeurophologyJ [14], MorphoNeuroNet [15], and the propagated skeleton approach [16], have also gained attention. Most fully automated analysis tools are typically based on rule-based segmentation algorithms. However, in recent years, we have witnessed a surge in research dedicated to cell segmentation using machine learning techniques, which has yielded many promising results. Some examples of machine learning-based cell segmentation algorithms include Cellpose (ver.2.2.3) [17] and Stardist (ver.0.8.5) [18], which offer the convenience of pre-trained models. Furthermore, these algorithms can be retrained to achieve highly accurate cell segmentation masks tailored to individual microscopic datasets [19]. In fact, a comprehensive cell analysis approach exists using machine learning-based cell segmentation [20].

The neuron images discussed in this paper are assumed to have been captured in a controlled lighting environment, without accounting for variations, such as low light conditions during nighttime. Nevertheless, the images in this study may exhibit haze and glare depending on the environmental conditions. The presence of haze and glare, which are characteristic of nighttime images, can be addressed by reviewing the previous relevant research [21–24].

One of the challenges when automatically analyzing neurons is that very few studies focus on bright-field images. Most of the methods mentioned above rely on the analysis of fluorescent images of cell nuclei and cytoplasm. However, since staining agents may impact cell integrity, the automated analysis of bright-field images is considered more advantageous. In recent years, highly accurate cell segmentation methods based on machine learning have become available, making cell segmentation from bright-field images feasible. However, bright-field cell images have a significant challenge in that it is difficult to detect only the neurite part since every component, such as the nuclei and neurites, is integrated into a single entity.

Therefore, this research proposes a novel approach to achieving the objective analysis of bright-field images using integrating machine learning-based cell segmentation with a graph structure representation of the neurons. This proposed graph structure enables more accurate neurite detection in the cell images. The primary contributions of this study can be summarized as follows:

- Analysis based on the bright-field images of cells;
- Analysis that specifically emphasizes the neurite structure of neurons;
- A rapid and objective fully automatic analysis process.

These contributions potentially serve to advance the understanding of the mechanisms underlying Alzheimer's disease and play a crucial role in the development of therapeutic and preventive interventions.

In this paper, we propose a new evaluation method for targeting neurons. This method involves retraining Cellpose using a pre-trained model in addition to representing cells as a graph structure using our proposed graphing technique. Subsequently, evaluation is conducted based on criteria like the maximum neurite length. Within the graphing method, quantification is performed using a single hyperparameter governing the internal region of the cell. To substantiate the efficacy of instance segmentation and the graphing method, we evaluate a variety of experiments to validate the analysis results related to rat adrenal pheochromocytoma PC12 cells and the Aβ content.

2. Materials and Methods

2.1. Reagents

Poly-D-Lysine was purchased from Sigma Aldrich (Laramie, WY, USA). Human Aβ42 (4349-v; Peptide Institute, Ibaraki, Japan) was purchased commercially. Nerve growth factor was purchased from Cosmo Bio (Tokyo, Japan).

2.2. Cell Culture

Rat adrenal pheochromocytoma PC12 cells were obtained from the JCRB Cell Bank (Ibaraki, Japan). The PC12 cells were maintained in DMEM (Wako, Osaka, Japan) supplemented with 10% fetal bovine serum (FBS) (Biowest, Nuaillé, France). Culture media were supplemented with 100 U/mL penicillin and 100 µg/mL streptomycin (Wakso). The cells were cultured at 37 °C in humidified air containing 5% CO_2.

2.3. Time-Lapse Observations

The PC12 cells were plated at 0.1×10^4 cells in a glass-bottom 96-well plate precoated with 0.1 mg/mL poly-D-lysine (Sigma Aldrich). The cells were incubated for 24 h. Then, after the removal of the culture medium, the wells were filled with DMEM/F12 (1:1) (Gibco, Billings, MT, USA) supplemented with 50 ng/mL NGF and defined as 0 h. The new medium included 1% DMSO or stepwise diluted $A\beta_{42}$ (5, 50, 500, 5.0×10^3, 5.0×10^4, 5.0×10^5, 5.0×10^6, 1.0×10^7 and 2.5×10^7 pM). For cell observation, time-lapse images were captured with an inverted microscope (Ti-E; Nikon, Tokyo, Japan) equipped with a color CMOS camera (DS-Ri2; Nikon) and an objective lens (PlanApo λ 20×/0.75 NA; Nikon). During observation, the cells were warmed in a chamber set at 37 °C in humidified air containing 5% CO_2. Images were captured every 15 min for 96 h and analyzed using NIS-Elements software (Nikon) (https://www.microscope.healthcare.nikon.com/products/software/nis-elements).

2.4. Manually Image Analysis

ImageJ software (NIH, Bethesda, MD, USA) was used to measure the projection length. The neurites were traced with a "segmented line". For the neurites that branched off in the middle, the longest part was traced from the root, and the rest were traced from the bifurcation point. The traced neurites were then labelled using the "ROI Manager" tool, and the physical lengths of all neurites were calculated. Incomplete cells located at the edge of the FOV were excluded from the analysis.

2.5. Image Processing

To process the bright-field images of neurons, the original RGB images were converted to grayscale images. For the quantitative evaluation of the neuron images, index masks were inferred using Cellpose. Next, the index masks were converted into graphs; we performed operations, including boundary estimation, skeletonizing, graphing, and the classification of nodes and edges. Finally, we evaluated metrics such as the neurite length.

2.5.1. Cell Segmentation

Cell segmentation is understood as instance segmentation applied to images depicting biological cells. Instance segmentation is a computer vision task that involves identifying

and separating individual objects within an image, including detecting the boundaries of each object and assigning a unique label to each one [25]. For example, Cellpose [17] and Stardist [18] are well-known cell segmentation algorithms. Cellpose is a U-Net-based cell segmentation algorithm that achieves highly accurate segmentation by specifying various parameters, such as the cell diameter (Figure 1). Cellpose supports a wide range of microscopic images, and Cellpose 2.0 [19] introduces human-in-the-loop optimization, enabling the attainment of highly accurate results. Therefore, in this paper, we utilize Cellpose for cell segmentation and enhance the accuracy of the pre-trained model through human-in-the-loop optimization.



(**a**) (**b**)

Figure 1. Cell Segmentation: (**a**) is a bright-field image of PC12 cell; (**b**) is a mask image of (**a**) using Cellpose.

2.5.2. Neuronal Graph Structure

The neuronal graph structure is a graphical representation of extracting the structure of a neuron. A typical neuron comprises a soma and neurites, which include axons and dendrites. We represent neuronal structures as mathematical graph structures, associating distinctive attributes with each node and edge (Figure 2). This method provides the precision and objectivity of neurite detection and allows the introduction of new evaluation metrics pertaining to neurites.

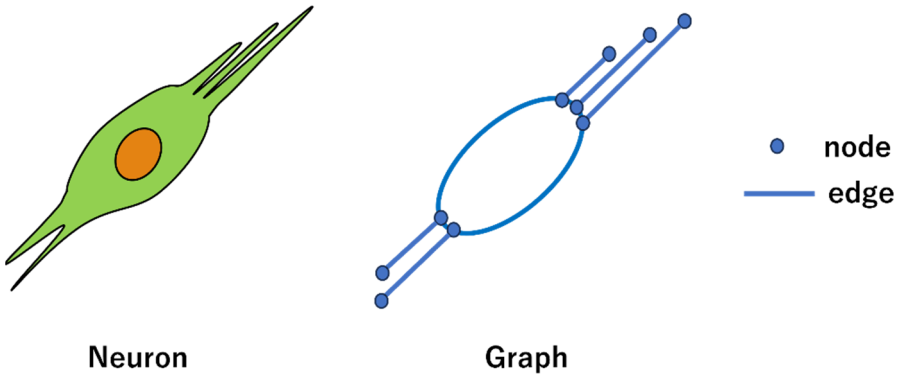


Figure 2. Relationship between neuron and graph: left is schematic diagram of neuron; right is graph structure.

The procedure for converting the mask data into neuronal graph structure consists of four steps.

1. Boundary estimation

In this step, we obtain the boundary of the neuron. We extract each cell (index) from the index mask and convert it into a binary map. On the binary map containing a single cell denoted with 1, we perform Euclidean distance transformation. Euclidean distance transformation is a projection that calculates the distance from each pixel with a value of 1 (neuron) to the nearest pixel with a value of 0 (background) and projects this distance onto a new map with the same dimensions. The result obtained via distance transformation is referred to as a distance map [26]. In our case, we utilized the Euclidean distance calculated with Equation (1) as the distance metric for distance transformation.

$$\mathrm{d}(p,q) = \sqrt{(p_x - q_x)^2 + (p_y - q_y)^2} \tag{1}$$

where d is the distance between p and q. p and q are arbitrary coordinates representing two points.

As a result, the maximum distance value R of the distance map can be determined. Additionally, the boundary is defined using the specified hyperparameter par ($0.0 < par < 1.0$) multiplied by R as a threshold (see Equation (2)).

$$\begin{aligned} R &= \max(dmap) \\ \text{Outer Area} &= \begin{cases} 0, & par \times R > dmap \\ 1, & par \times R \leqq dmap \end{cases} \end{aligned} \tag{2}$$

where R is the maximum value of the distance map. $dmap$ is the distance map. The outer area is the data after the process.

Based on the results of preliminary comparative experiments involving various distance metrics, we chose to employ Euclidean distance as the preferred distance metric. This choice was made due to the Euclidean distance exhibiting a more precise representation of the distance to the neuronal center. The image after this process is shown in Figure 3b.

2. Skeletonization

In this step, the boundary obtained in step 1 is skeletonized. During the skeletonization process, the boundary is reduced to a few lines, and the shapes of the soma and neurites are retrieved. While there are various skeletonization methods available, this paper employs the most used thinning algorithm, the Zhang–Suen algorithm [27]. The Zhang–Suen Thinning algorithm was introduced in 1984 and has become the most widely adopted and thoroughly validated technique, primarily due to its robustness. And there is also research aimed at improving the processing speed using this algorithm [28].

The skeletonized boundary is presented in Figure 3c.

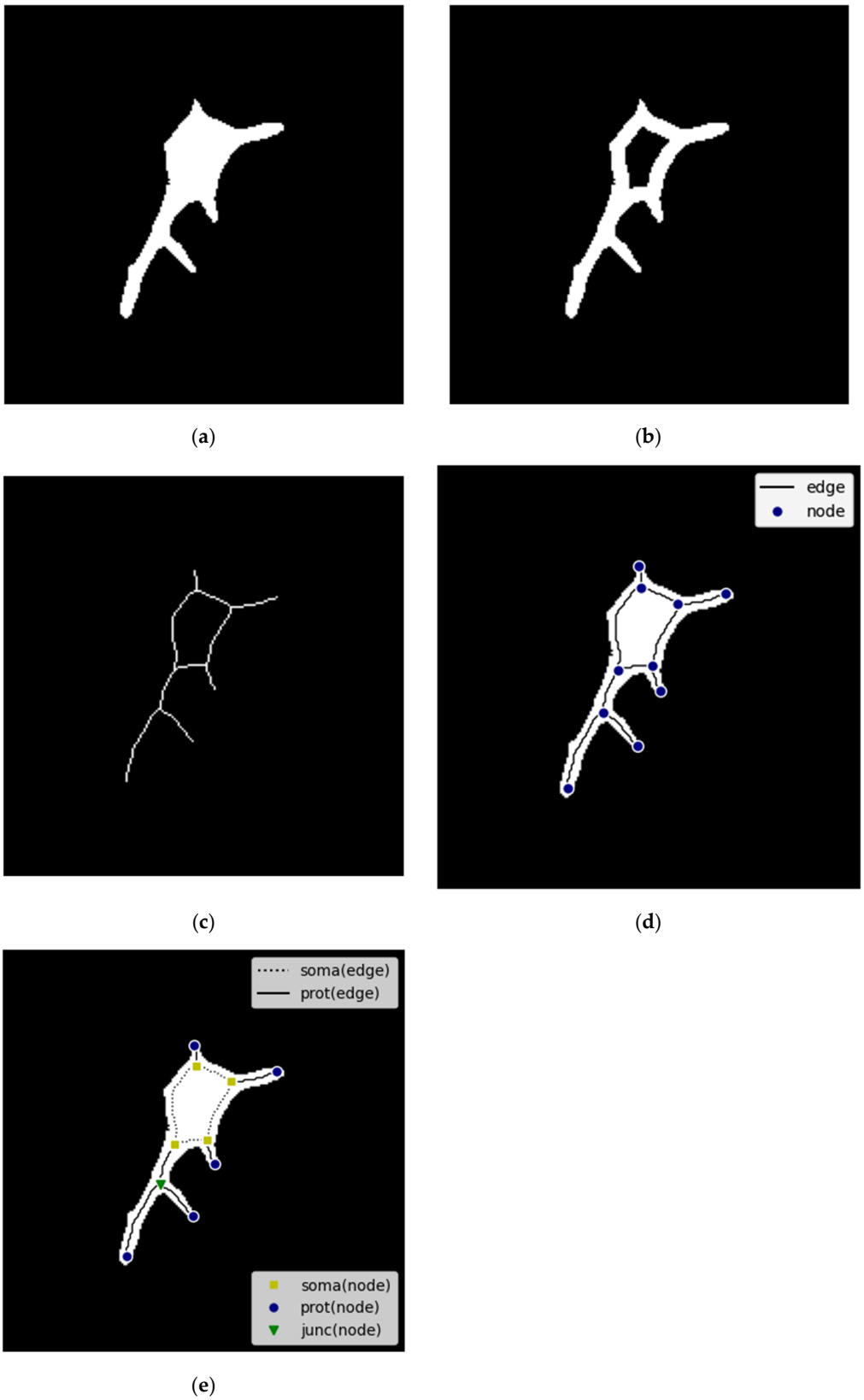
3. Graphing

This step involves converting the skeletonized data into a graph structure. The graph creation method follows sknw [29], a submodule of ImagePy [30]. This module constructs nodes and edges from the thinned data and converts it into a Python graph library networkX.

The process of graph conversion is based on the skeletonizing function. The initial focus is on pixel 1 (neuron) within the skeletonized image. When examining the eight neighboring pixels of that point, if there is exactly 1 node with a value of 1 (neuron), that pixel is identified as an edge contributing to the graph. In cases where there is not exactly such a node, they are designated as either edges or nodes that constitute the graph. Additionally, the classification of these edges and nodes is further refined based on their isolation. Finally, the graph is constructed by tracing the eight nearest neighbors of each edge and node.

Furthermore, the graph structure is represented as a multigraph, allowing multiple edges between nodes. If it is not a multigraph, it may not be possible to obtain the structure of the neuron, for example, when two neurites emerge from different nodes.

The image after the thinning process is shown in Figure 3d.



(**a**) (**b**) (**c**) (**d**) (**e**)

Figure 3. Image of graph process. (**a**) Bright-field image of PC12 cell (identical to Figure 1b). (**b**) Outer area image in (**a**). (**c**) Image after skeletonizing processing in (**b**). (**d**) Image after graphing processing in (**c**). (**e**) is the image after the classification of nodes and edges in (**d**).

4. Classifying nodes and edges

Finally, the graph data are linked to the neuron, and each node and edge are classified according to the correspondence between the neuron and the graph structure.

- Nodes
  - Soma node;
  - Protrusion node;
  - Junction node.
- Edges
  - Soma edge;
  - Protrusion edge.

To classify these nodes and edges, we first locate closed loops within in the graph, which are associated with the cell body. Therefore, the nodes included this loop are defined as body nodes, and the edges are defined as body edges. Next, we find a node that has not yet been classified and has a degree of 1 and define that node as a protrusion node. Finally, remaining nodes defined as branch nodes, and unlabeled edges are defined as protruding edges. Through this procedure, information about neurons and graph structures is interconnected, allowing the neurons to be schematically represented as a graph structure.

$$\text{Nodes} = \begin{cases} \text{Soma Node}, & \text{if node that composd of loop} \\ \text{Protrusion Node}, & \text{elif node degree is 1} \\ \text{Junction Node}, & \text{otherwise} \end{cases} \tag{3}$$

$$\text{Edges} = \begin{cases} \text{Soma Edge}, & \text{if edge that composd of loop} \\ \text{Protrusion Edge}, & \text{otherwise} \end{cases} \tag{4}$$

where the nodes are all the nodes of a cell. Edges are all the edges of a cell. The soma node, protrusion node, junction node, soma edge, and protrusion edge are the names of the nodes and edges after classification.

The image after this process is shown in Figure 3e.

2.5.3. Quantitative Evaluation

In the quantitative evaluation, the evaluation metrics for neurons are established and assessed. First, the neurite length is estimated as the distance between the node representing the tip of the neurite and the node denoting the border between the neurite and the cell body. The number of neurite length instances is defined by the number of protrusion nodes. This is determined using Equation (5).

$$\text{Neurite Length}(x) = \min_{i \in \mathrm{I}} \text{dist}(x, y_i) \tag{5}$$

where the neurite length(x) describes the neurite length up to node x from the soma. Variable x is any $\text{node}_{\text{prot}}$, while variable y is all the $\text{Nodes}_{\text{soma}}$.

Further, the maximum neurite length can be calculated using Equation (6), and the total neurite length can be calculated using Equation (7).

$$\text{Max Neurite Length} = \max\left(\text{Nurite Lengths}\right) \tag{6}$$

$$\text{Total Neurite Length} = \text{sum}\left(\text{Edges}_{\text{prot}}\right) \tag{7}$$

where the maximum neurite length is the maximum length of a neurite extending from one neuron. The total neurite length is the sum length of a neurite extending from one neuron. The neurite length is a set that represents the lengths of each neurite extending from a single neuron. $\text{Edges}_{\text{prot}}$ is a set that represents the protrusion edges.

Finally, the number of neurite tips can be calculated using Equation (8), and the number of neurite roots can be calculated using Equation (9).

$$\text{Neurite tip} = \text{Nodes}_{\text{prot}} \tag{8}$$

$$\text{Neurite foot} = \begin{cases} \text{None}\,, & \text{len}\left(\text{Edges}_{\text{prot}}\right) = 0 \\ \text{Nodes}_{\text{soma}}, & \text{len}\left(\text{Edges}_{prot}\right) \neq 0 \end{cases} \tag{9}$$

where the neurite tip represents the number of individual neurite tips, and the neurite foot represents the number of individual neurite bases. The term none denotes the absence of a neurite. $\text{Edges}_{\text{prot}}$ is a set that represents the protrusion nodes.

By expressing it as a graph, it is also possible to calculate indicators such as the curvature of each neurite. However, in this article, we have focused on simple and very important metrics. The purpose of this paper is to first demonstrate the validity of the analysis expressed as a graph. Therefore, in this study, we focused on the neurite length, number of neurite tips, and number of neurite roots as metrics of neurite measurement.

To visualize the analytical data related to these evaluation metrics, time was plotted along the horizontal axis, while the value of evaluation indicators is depicted along the vertical axis. Previously, a significant portion of this analysis was conducted manually, consuming substantial time to evaluate the fixed time points (e.g., 0 h, 24 h, and 48 h). However, with the advent of automation, the process can now be executed efficiently, enabling the rapid processing of huge image datasets.

3. Results

3.1. Approach Validation of Cell Segmentation

First, we verified cell segmentation. This time, we used Cellpose 2.0, which is one of the cell segmentation algorithms. Cellpose 2.0 allows retraining using "human-in-the-loop" and allows you to create a model tailored to your data. Therefore, we retrained the model on about 50 of the image data (500 ROI) using livecell [31] from among the pretrained models prepared in advance. Training was performed within the Cellpose GUI app, with the following settings.

Learning settings

- Initial model: livecell;
- chan: gray;
- chan2: none;
- learning rate: 0.01;
- weight decay: 0.0001;
- *n* epochs: 1000.

We define this model as our model and compared it with the pre-trained models cyto2 and livecell. We prepared 21 test annotations and attempted evaluations using four evaluation metrics: precision, recall, IoU, and F-measure. Table 1 below shows the results.

Table 1. Comparison of our model and the pre-trained model.

	Precision	**Recall**	**IoU**	**F-Measure**
Cyto2	0.799	0.831	0.682	0.806
livecell	0.727	0.814	0.610	0.750
Our model	0.865	0.891	0.781	0.876

As shown in Table 1, our model achieved better results for all the evaluation metrics.

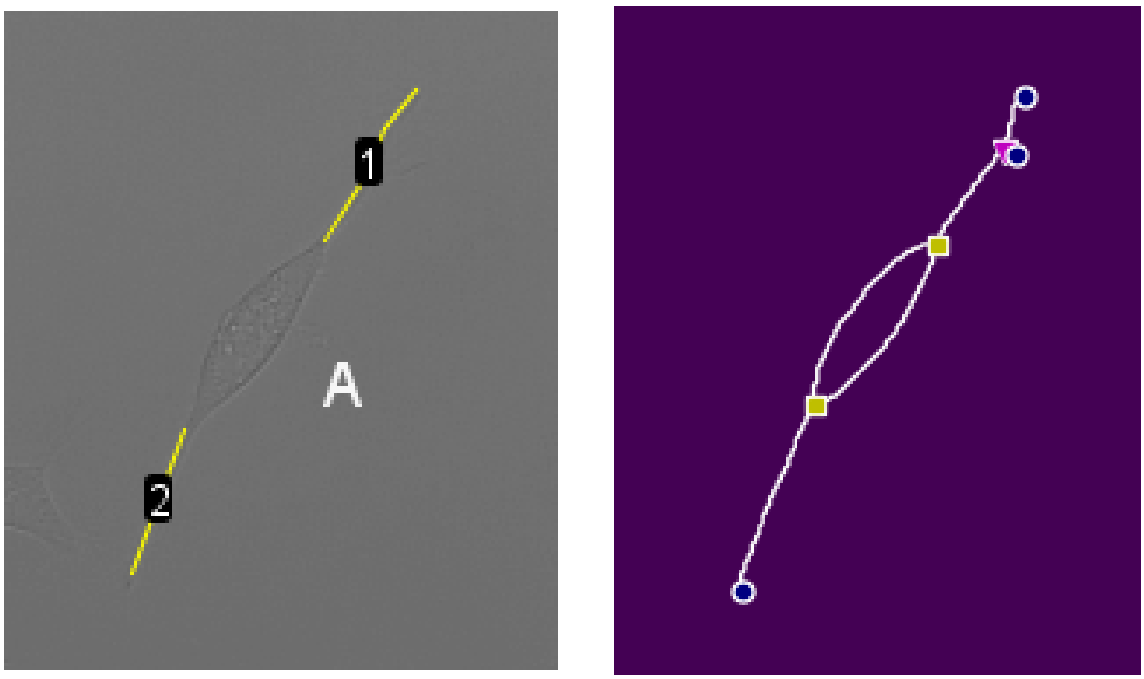
However, there were cases in which detection was difficult using all the models. For example, when the brightness was low, when there was a lot of dust, or when cells overlapped or were largely adhered to each other, the accuracy of segmentation decreased.

And, although cells from 0 h to 48 h could be successfully detected in many cases, the cells from 48 h onwards were difficult to detect. However, the results were better than those of the pre-trained model and were able to accurately capture the cell contour for up to 48 h, making it possible to perform analysis using these data.

3.2. Neuronal Graph Structure Neuronal Graph Structure Neuronal Graph Structure Approach Validation

Next, we verified the neurite graph structure. This graphing method uses a hyperparameter when determining the internal region of a cell. As a result of preliminary verification, it was confirmed that the results did not change significantly in the range from 0.4 to 0.6, so, here, we fixed the hyperparameter value at 0.5 and compared it with the analysis results of the actual humans.

As a verification method, in total, we extracted 71 neurites from all the images and compared the measurement results of the proposed method with manual analysis using ImageJ. Human analysis was performed using ImageJ, and analysis was performed using the steps presented in Section 2.4 (Figure 4). The neurites extracted for this verification were determined to be neurites by both the humans and the proposed algorithm.



(**a**) (**b**)

Figure 4. (**a**) Manual analysis using ImageJ. (cell labels are represented by alphabets (A, B, C), and neurite labels are represented by numbers (1, 2, 3)) (**b**) Graph structure representation of neurons using the proposed method. (The meaning of the node is the same as in Figure 3).

Figure 5 shows the comparison results of neurite length. The mean absolute error was 4.387 µm. When comparing the neurite lengths, the regression line between the manual neurite length measurement (ImageJ) and the automatic analysis (Presented approach) was $y = 0.977x + 2.129$. The coefficient of determination was $R^2 = 0.9372$, which indicates a strong correlation between the manual measurement length (ImageJ) and the automated analysis (the presented approach). In addition, when considering neurites longer than 40 µm or more, which is important during analysis, the average error ratio of length was 0.11. In summary, the presented graphing method matches the result of manual neurite length estimation.

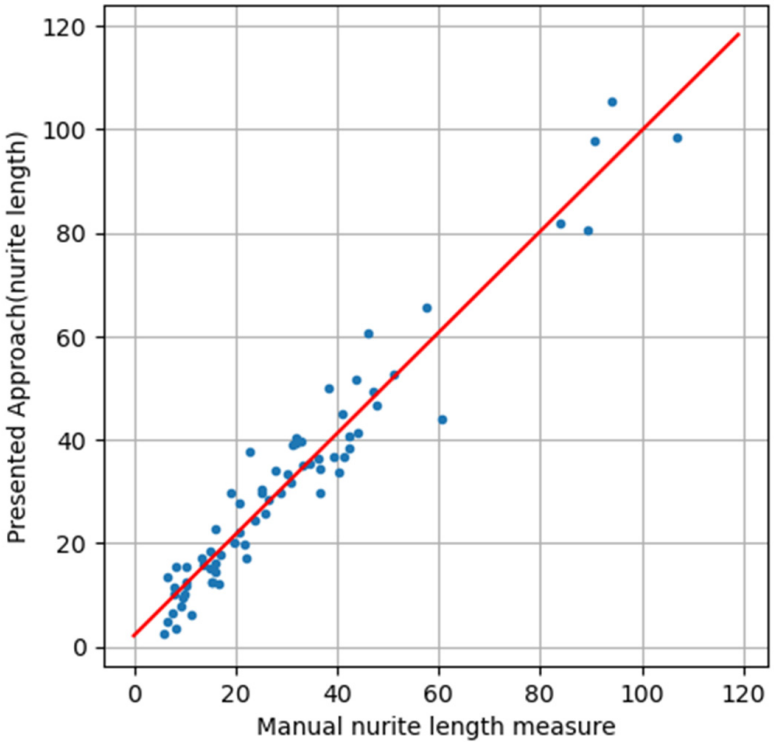


Figure 5. Correlation between manual analysis and the proposed method.

3.3. Aβ Dependence

Finally, we added various concentrations of Aβ to the individual PC12 cell cultures. This assessment encompassed the systematic observation of cellular images over a defined time frame in reaction to different concentrations of Aβ.

Aβ concentrations

- 5 pM;
- 50 pM;
- 500 pM;
- 5 nM;
- 50 nM;
- 500 nM;
- 5 μM;
- 10 μM.

Times

- 0 h;
- 24 h;
- 48 h;
- 72 h;
- 96 h.

In this experimental procedure, we derived the results by averaging the values of all the neurite lengths from three different bright-field images for each condition. Figure 6 and Table 2 illustrates the outcomes, as presented below.

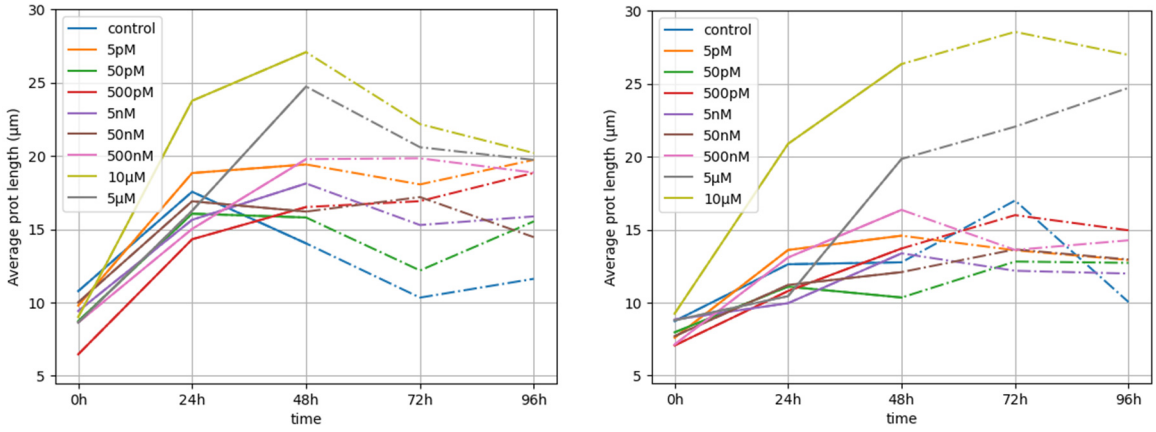


Figure 6. (**a**) Changes in average neurite length of Aβ-treated PC12 cells for 96 h using the proposed method. (**b**) ImageJ analysis results of changes in average neurite length of Aβ-treated PC12 cells for 96 h.

Table 2. Mean error of Figure 6.

	0 h	24 h	48 h	72 h	96 h
Mean Error (±μm)	1.04	2.78	1.90	3.25	3.01

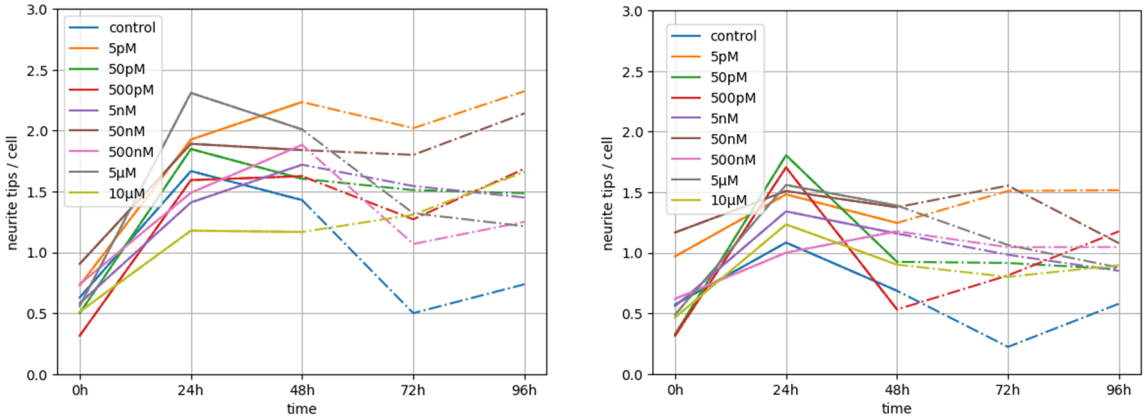
Initially, at 0 h, both the measured values fell within the range of approximately 10 μm, with an average error of ±1.04 μm. Further, the accuracy of neurite detection using the cell segmentation and graphical techniques where confirmed visually, yielding results that are largely consistent with the manual measurements.

At 24 h, the highest concentration (10 μM) induced significant neurite extensions, particularly in the regions where no substantial change was observed at other concentrations. However, it is noteworthy that the measured values generally exceeded those of manual analysis, indicating a propensity for detecting longer neurites, with an average deviation of +2.78 μm.

The distinctive outcomes at 10 μM remained within an acceptable margin of error, affirming the significant extension of neurites at this concentration. Subsequently, at 48 h, both the 5 μM and 10 μM concentrations exhibited considerable neurite extension, which align closely with the manual analysis results.

Nonetheless, the results deviated at 72 h and 96 h, where the length of the neurites at 5 μM and 10 μM diminished in contrast to the manual analysis data. The average error also increased when surpassing 3 μm. Visual verification attributed this discrepancy to the influence of the cell segmentation approach. These findings suggest that the cell segmentation method employed in this study is effective for an automated analysis approach up to approximately 48 h. However, we anticipate improvement in the future. The primary limitation pertains to cell segmentation, and we anticipate enhancing the accuracy through the extensive retraining of Cellpose using a more extensive training dataset or by developing and implementing a new segmentation model. An additional advantage of incorporating cell graphs is the ability to represent cells as a schematic structure, opening the door for enhanced cell segmentation and the introduction of novel evaluation metrics in future research.

Next, we conducted the comparative analysis of the neurite tip count results. It is important to note that all the cell counts used to calculate the average were determined using ImageJ. This approach was employed only for comparing the number of tips, as both the automatic and manual detection methods can introduce significant discrepancies in the cell counts. Figure 7 and Table 3 illustrates the outcomes, as presented below.



(**a**) (**b**)

Figure 7. (**a**) Average number of neurite tips per cell of Aβ-treated PC12 cells for 96 h using the proposed method. (**b**) ImageJ analysis results for the changes in the average number of neurite tips per cell of Aβ-treated PC12 cells for 96 h.

Table 3. Mean error of Figure 6.

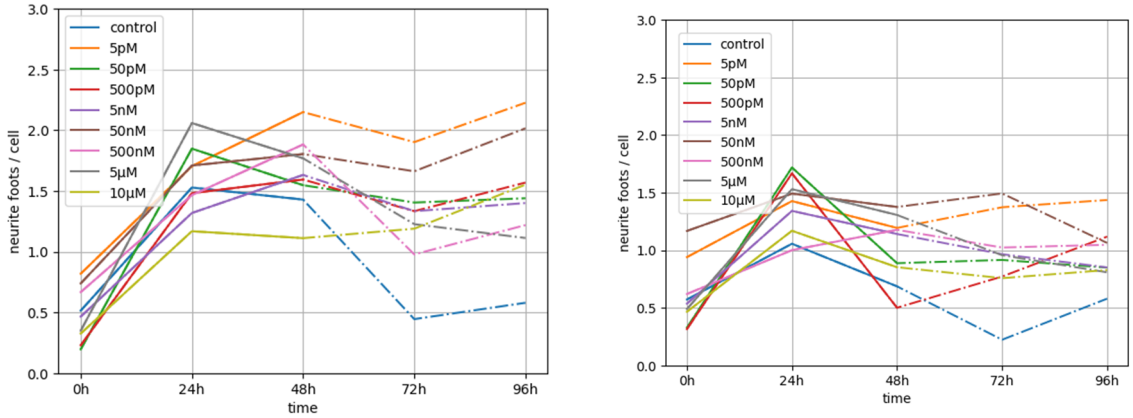
	0 h	**24 h**	**48 h**	**72 h**	**96 h**
Mean Error	0.11	0.32	0.68	0.38	0.56

Firstly, at the 0 h time point, both the measurements fell within a range of approximately 0.7 ± 0.5, with an average deviation of ± 0.11. This observation is similar to the outcomes of manual analysis.

Subsequently, after 24 h, the results indicate an increase in all the concentrations, aligning with manual analysis trends. However, it is noteworthy that the measured values generally surpassed those of the manual analysis, with a mean deviation of 0.32. This pattern is like the neurite length analysis results in Experiment 3.1 and implies the acquisition of finer neurites compared to those of manual analysis. A similar result is that most of the 48 h analysis results remained the same without significant changes.

From the comparison, we conclude that when the cell segmentation approach exhibits a sufficient accuracy, there are no significant disparities between the analysis results, and the trends between the automatic and manual analyses are very similar. It is important to note that the error temporarily declines at 72 h, and then increases at 96 h. We attribute this fluctuation to the number of detected cells. After 72 h, the cell segmentation approach of the automatic analysis approach might face challenges, leading to a temporary decline in accuracy. Subsequently, the error rises as the number of detected cells increases.

Finally, we conducted the comparative analysis of the neurite root count results. The same method used for analyzing the number of protrusion tips was used for this measurement. Figure 8 and Table 4 illustrates the outcomes, as presented below.



(**a**) (**b**)

Figure 8. (**a**) Average number of neurite roots per cell of Aβ-treated PC12 cells for 96 h using the proposed method. (**b**) ImageJ analysis results in changes in the Average number of neurite roots per cell of Aβ-treated PC12 cells for 96 h.

Table 4. Mean error of Figure 6.

	0 h	**24 h**	**48 h**	**72 h**	**96 h**
Mean Error	0.13	0.25	0.64	0.34	0.50

The analysis results for the neurite roots are very similar to the outcomes obtained for the number of neurite tips. Consequently, the same conclusions drawn for the neurite tips can be extended to the analysis results for the neurite roots. Moreover, the average error between the number of neurite tips and roots in automatic analysis is 0.045, and the error in manual analysis is also very small. This highlights the similarities between the automated and manual analyses, showing that the rules for both are precisely defined and have a minimal impact on the analysis results.

4. Discussion

The main contribution of this research lies in the introduction of an original and automatic analysis method specifically designed for the evaluation of neurites in neurons. By comparing the measurements of the neurite length, we have demonstrated that our method can yield neurite length analysis results that are comparable to those obtained through manual analysis. Furthermore, we have validated the capability of conducting highly precise neurite length analysis for up to 48 h when working with single images. Additionally, our results align with manual analysis regarding the quantification of neurite tips and roots. These findings collectively offer significant potential for expediting and enhancing the objectivity when analyzing neuronal characteristics.

However, the method does have limitations, in particular, caused by the cell segmentation accuracy. Specifically, when dealing with a high cell density, there is a significant increase in cell overlap, which subsequently leads to less-precise segmentation.

Nevertheless, we believe that these issues can be addressed by enhancing the accuracy of cell segmentation. One specific approach is to further explore Cellpose, a cutting-edge tool for cell segmentation. By retraining it, we may achieve highly accurate segmentation even in environments with substantial cell proliferation. Alternative segmentation models, such as Stardist, or the development of a custom cell segmentation model could also be considered. The choice of segmentation method may depend on the characteristics of the cell images, offering the potential to achieve an even greater analysis accuracy than what is currently available.

5. Conclusions

This paper introduced an innovative and automated analysis approach for bright-field images of neurons, with a specific focus on assessing neurite activity using advanced cellular segmentation techniques. We represent neuronal structures as schematic graphs, employing contour estimation, thinning, and graphing techniques to accurately identify neurite features within the cells. To validate the accuracy of our proposal approach, we compared the results of this method to the manual analysis (ImageJ) of the neurite length of rat adrenal pheochromocytoma PC12 cells. The comparisons revealed a notable level of agreement, with a limited average error of ± 4.387 µm. Despite the persisting challenges in cell segmentation, we have effectively depicted changes in the neurite length over time, with the results remaining consistent with the manual measurements for the first 48 h. Due to these results, we believe that our proposed approach holds the potential to significantly advance the field of neuronal research. It offers a powerful tool for the automated analysis of neurite activity in bright-field images, thereby contributing to our understanding of neuronal processes and their relevance to neurodegenerative diseases such as Alzheimer's disease.

Author Contributions: Conceptualization, F.C. and S.W.; methodology, F.C., S.W. and S.B.; software, F.C.; validation, F.C. and A.O.; formal analysis, F.C. and A.O.; investigation, F.C., A.O. and M.K.; data curation, F.C., A.O., M.K. and K.T.; supervision, S.W. and K.T. All authors participated in writing the manuscript. All authors have read and agreed to the published version of the manuscript.

Funding: This work was supported by JST Grant Number JPMJPF2213.

Data Availability Statement: The data that support the findings of this study are available from the corresponding author, Fumiya Chikudo, upon reasonable request.

Conflicts of Interest: The authors declare no conflict of interest.

References

1. Alzheimer, A. A new disease of the cortex. *Allg. Z. Fuer Psychiatr. Und Psych. Gerichtl. Med.* **1907**, *64*, 146–148.
2. Hippius, H. The discovery of Alzheimer's disease. *Dialogues Clin. Neurosci.* **2003**, *5*, 101–108. 480. [CrossRef] [PubMed]
3. Association, A. Alzheimer's disease facts and figures. *Alzheimers Dement.* **2015**, *11*, 332–384. [CrossRef]
4. Scheltens, P. Alzheimer's disease. *Lancet* **2016**, *388*, 505–517. [CrossRef] [PubMed]
5. Dobson, C.M. *The Amyloid Phenomenon and Its Links with Human Disease*; ColdSpring Harbor ab Press: Cold Spring Harbor, NY, USA, 2017; pp. 1–14. [CrossRef]
6. Koo, E.H. Amyloid diseases: Abnormal protein aggregation in neurodegeneration. *Proc. Natl. Acad. Sci. USA* **1999**, *96*, 9989–9990. [CrossRef]
7. Das, K.P.; Freudenrich, T.M.; Mundy, W.R. Assessment of PC12 cell differentiation and neurite growth: A comparison of morphological and neurochemical measures. *Neuro. Toxicol. Teratol.* **2004**, *26*, 397–406. [CrossRef]
8. Obin, M.; Mesco, E.; Gong, X.; Haas, A.L.; Joseph, J.; Taylor, A. Neurite outgrowth in PC12 cells: Distinguishing the roles of ubiquitylation and ubiquitin-dependent proteolysis. *J. Biol. Chem.* **1999**, *274*, 11789–11795. [CrossRef]
9. Koch, K.; Bartmann, K.; Hartmann, J.; Kapr, J.; Klose, J.; Kuchovská, E.; Pahl, M.; Schlüppmann, K.; Zühr, E.; Fritsche, E. Scientific Validation of Human Neurosphere Assays for Developmental Neurotoxicity Evaluation. *Front. Toxicol.* **2022**, *4*, 816370. [CrossRef]
10. Radler, M.R.; Liu, X.; Peng, M.; Doyle, B.; Toyo-Oka, K.; Spiliotis, E.T. Pyramidal neuron morphogenesis requires a septin network that stabilizes filopodia and suppresses lamellipodia during neurite initiation. *Curr. Biol.* **2023**, *33*, 434–448.e8. [CrossRef]
11. Abramoff, M.D.; Magelhaes, P.J.; Ram, S.J. Image Processing with ImageJ. *Biophotonics Int.* **2004**, *11*, 36–42.
12. Carpenter, A.E.; Jones, T.R.; Lamprecht, M.R.; Clarke, C.; Kang, I.H.; Friman, O.; Guertin, D.A.; Chang, J.H.; Lindquist, R.A.; Moffat, J.; et al. CellProfiler: Image analysis software for identifying and quantifying cell phenotypes. *Genome Biol.* **2006**, *7*, R100. [CrossRef] [PubMed]
13. Pool, M.; Thiemann, J.; Bar-Or, A.; Fournier, A.E. NeuriteTracer: A novel ImageJ plugin for automated quantification of neurite outgrowth. *J. Neurosci. Methods* **2008**, *168*, 134–139. [CrossRef]
14. Ho, S.Y.; Chao, C.Y.; Huang, H.L.; Chiu, T.W.; Charoenkwan, P.; Hwang, E. NeurphologyJ: An automatic neuronal morphology quantification method and its application in pharmacological discovery. *BMC Bioinform.* **2011**, *12*, 230. [CrossRef] [PubMed]
15. Pani, G.; Vos, W.H.; Samari, N.; Saint-Georges, L.; Baatout, S.; Oostveldt, P.; Benotmane, M.A. MorphoNeuroNet: An automated method for dense neurite network analysis. *Cytom. Part A* **2014**, *85*, 188–199. [CrossRef] [PubMed]
16. Schikora, J.; Kiwatrowski, N.; Förster, N.; Selbach, L.; Ostendorf, F.; Pallapies, F.; Hasse, B.; Metzdorf, J.; Gold, R.; Mosig, A.; et al. A propagated skeleton approach to high throughput screening of neurite outgrowth for in vitro Parkinson's disease modelling. *Cells* **2021**, *10*, 931. [CrossRef]

17. Stringer, C.; Wang, T.; Michaelos, M.; Pachitariu, M. Cellpose: A generalist algorithm for cellular segmentation. *Nat. Methods* **2021**, *18*, 100–106. [CrossRef]
18. Schmidt, U.; Weigert, M.; Broaddus, C.; Myers, G. Cell Detection with Star-Convex Polygons. In Proceedings of the Medical Image Computing and Computer Assisted Intervention, 2018–21st International Conference, Granada, Spain, 16–20 September 2018; pp. 265–273. [CrossRef]
19. Pachitariu, M.; Stringer, C. Cellpose 2.0: How to train your own model. *Nat. Methods* **2022**, *19*, 1634–1641. [CrossRef]
20. Baar, S.; Kuragano, M.; Tokuraku, K.; Watanabe, S. Towards a comprehensive approach for characterizing cell activity in bright-field microscopic images. *Sci. Rep.* **2022**, *12*, 16884. [CrossRef]
21. Kuanar, S.; Mahapatra, D.; Bilas, M.; Rao, K.R. Multi-path dilated convolution network for haze and glow removal in nighttime images. *Vis. Comput.* **2022**, *38*, 1121–1134. [CrossRef]
22. Wang, W.; Wang, A.; Liu, C. Variational Single Nighttime Image Haze Removal with a Gray Haze-Line Prior. *IEEE Trans. Image Process.* **2022**, *31*, 1349–1363. [CrossRef] [PubMed]
23. Liu, Y.; Yan, Z.; Tan, J.; Li, Y. Multi-Purpose Oriented Single Nighttime Image Haze Removal Based on Unified Variational Retinex Model. *IEEE Trans. Circuits Syst. Video Technol.* **2023**, *33*, 1643–1657. [CrossRef]
24. Liu, Y.; Yan, Z.; Chen, S.; Ye, T.; Ren, W.; Chen, E. Nighthazeformer: Single nighttime haze removal using prior query transformer. In Proceedings of the 31st ACM International Conference on Multimedia, Ottawa, ON, Canada, 29 October 2023–3 November 2023; pp. 4119–4128. [CrossRef]
25. Instance Segmentation, Papers with Code. Available online: https://paperswithcode.com/task/instance-segmentation (accessed on 10 October 2023).
26. Strutz, T. The distance transform and its computation. *arXiv* **2021**. [CrossRef]
27. Haralick, R.M. A Fast Parallel Algorithm for Thinning Digital Patterns. *Image Process. Comput. Vis.* **1984**, *27*, 236–239. [CrossRef]
28. Chen, W.; Sui, L.; Xu, Z.; Lang, Y. Improved zhang-suen thinning algorithm in binary line drawing applications. In Proceedings of the International Conference on Systems and Informatics (ICSAI2012), Yantai, China, 19–20 May 2012; pp. 1947–1950. [CrossRef]
29. Yan, X.; Charles, N.C. Sknw: Build Network from Skeleton Image (2D-3D) (2017), Version 0.13. Available online: https://github.com/Image-Py/sknw (accessed on 1 October 2023).
30. Wang, A.; Yan, X.; Wei, Z. ImagePy: An open-source, Python-based and platform-independent software package for bioimage analysis. *Bioinformatics* **2018**, *34*, 3238–3240. [CrossRef] [PubMed]
31. Edlund, C.; Jackson, T.R.; Khalid, N.; Bevan, N.; Dale, T.; Dengel, A.; Ahmed, S.; Trygg, J.; Sjögren, R. LIVECell—A large-scale dataset for label-free live cell segmentation. *Nat. Methods* **2021**, *18*, 1038–1045. [CrossRef] [PubMed]

Disclaimer/Publisher's Note: The statements, opinions and data contained in all publications are solely those of the individual author(s) and contributor(s) and not of MDPI and/or the editor(s). MDPI and/or the editor(s) disclaim responsibility for any injury to people or property resulting from any ideas, methods, instructions or products referred to in the content.